

Analysis of fracture in thin shells by overlapping paired elements

Pedro M.A. Areias, J.H. Song, Ted Belytschko *

Department of Mechanical Engineering, Northwestern University, 2145 Sheridan Road, Evanston, IL 60208-3111, USA

Received 18 April 2005; received in revised form 12 October 2005; accepted 14 October 2005

Abstract

A finite element methodology for evolution of cracks in thin shells using mid-surface displacement and director field discontinuities is presented. We enrich the mid-surface displacement and director fields of a discrete Kirchhoff–Love quadrilateral element using a piecewise decomposition of element kinematics, which leads to a basis that is a variant of the one used in the extended finite element method. This allows considerable simplifications in the inclusion of the shell director field. A cohesive law is employed to represent the progressive release of the fracture energy. In contrast with previous works, we retain the original quadrature points after the formation of a crack, which, in combination with an elasto-plastic multiplicative decomposition of the deformation gradient, avoids the previously required internal variable mapping during crack evolution. Results are presented for large strain elastic and elasto-plastic crack propagation.

© 2005 Elsevier B.V. All rights reserved.

Keywords: Fracture; Elasto-plasticity; Shell elements; Extended finite element method

1. Introduction

Argyris' study of large rotations [1] has had a profound impact on finite element methods for large displacements of shells. It provided a consistent framework for treating large deformation of shells and beams and influenced later work such as Simo et al. [2,3] and Ramm and co-workers [4–6]. In this paper we describe a Kirchhoff–Love shell element for arbitrary crack propagation that employs large rotations about moving axis. This work is motivated by a previous method we developed for fracture in plate and shell structures using the extended finite element method (XFEM) [7]. Two difficulties became apparent during the course of that work. One was the relatively non-trivial incorporation of the director field enrichment. Another was the difficulty in formulating a cohesive law with transverse shear stress components. Here we describe a discrete Kirchhoff–Love element (see also [8]), for crack propagation. We use a reinterpretation of the XFEM methodology which leads to a formulation similar to the Hansbo and Hansbo [9] approach to discontinuities (see also [10]). The introduction of a displacement discontinuity in a discrete Kirchhoff–Love element is surprisingly straightforward using this technique. With a number of proposed considerations, it is possible to add crack propagation to an existing finite element code with minimal modifications. Very little has been done on arbitrary progressive fracture in plates and shells. Dolbow et al. [11] considered non-propagating cracks in plates by XFEM. An inter-element cracking formulation for shells was recently proposed by Cirak et al. [12] using cohesive elements, in the explicit dynamics context. Lee et al. [13] employed commercial codes and element deactivation to model circular fracture in punched plates.

We describe some details of this shell finite element and provide a more general formulation of the fracture model. The elasto-plastic framework adopted is based on Lee's [14] multiplicative decomposition of the deformation gradient and an unsymmetric return mapping algorithm, proposed here (see also [15]).

* Corresponding author. Tel.: +1 847 491 4029; fax: +1 847 491 4011.

E-mail address: tedbelytschko@northwestern.edu (T. Belytschko).

shows these sub-domains, along with two parts of the crack surface corresponding to the constrained (Γ_{0a}) and unconstrained (Γ_{0b}) crack surface. The crack surface partition is defined as $\Gamma_0 = \Gamma_{0a} \cup \Gamma_{0b}$ with $\Gamma_{0a} \cap \Gamma_{0b} = \emptyset$. According to the sub-domain, we consider two distinct deformation maps $\varphi^- : \Omega_0^- \ni X^- \mapsto x^- \in \Omega^-$ and $\varphi^+ : \Omega_0^+ \ni X^+ \mapsto x^+ \in \Omega^+$ and the additional condition: $X \in \Gamma_{0a} \Rightarrow \varphi^+(X) \equiv \varphi^-(X)$. In the sub-domain Γ_{0b} the deformation maps can assume distinct values. With the graphical representation of Fig. 1 we can interpret the crack as the part of Γ for which $\varphi^+ \neq \varphi^-$. We can define $\Gamma_a = \varphi(\Gamma_{0a})$ and, for Γ_{0b} , $\Gamma_b^+ = \varphi^+(\Gamma_{0b})$ and $\Gamma_b^- = \varphi^-(\Gamma_{0b})$. In other words, a cracked configuration can be viewed as two pristine configurations with a common domain (denoted here as Γ_a).

One can observe that, in terms of kinematics, no substantial difference exists between a cracked body and an un-cracked one. It is also noteworthy that when a discretization is carried out, unless the crack path is known a priori, the crack path Γ_b would not coincide with finite elements edges. To deal with this fact, we use the following procedure. For each element containing a given part of Γ_{0b} , which we will denote as $\mathbb{P}(\Gamma_{0b})$, we use a superposition of two elements with common parts in Ω^+ and Ω^- , but one associated with the deformation map φ^+ and the other one associated with φ^- . Although this interpretation by itself is not new (see, e.g. [9]), it naturally allows a formulation of cracked rods and shells with distinct director fields (\mathbf{n}^+ and \mathbf{n}^- in Fig. 1) circumventing the association of these with an underlying (un-cracked) shell as was done in our previous work [8].

An interpretation for a beam is provided in Fig. 2. Note that the representation of the directors in the deformed configuration follows from independent deformation maps. Making use of the Heaviside function H , we can write $H[f(X)] = 0$ for $X \in \Omega_0^-$ and $H[f(X)] = 1$ for $X \in \Omega_0^+$. We also introduce the nodal quantities $H_K = H[f(X_K)]$ (with K being the node number) as

$$H_K = \begin{cases} 0, & X_K \in \Omega_0^-, \\ 1, & X_K \in \Omega_0^+. \end{cases} \quad (1)$$

The element (see [8]) on which we have implemented the current developments is represented in Fig. 3. The element contains 4 corner nodes where the displacement (and position) is interpolated and 4 mid-side nodes for rotation interpolation. The implementation details are given in Ref. [8]. The mid-side rotation degrees of freedom are denoted as β_L with $L = \text{I}, \dots, \text{IV}$ (Roman numerals are employed for the mid-side variables, as in [8]). The corner nodes position degrees of freedom are denoted as r_K with $K = 1, \dots, 4$ and these nodes are used for the mid-surface displacements.

For the cracked elements, we use two superimposed displacement and director fields. We employ the notation r_K and β_L for standard degrees of freedom and r_K^* and β_L^* for the enriched degrees of freedom, respectively. Let us now discuss the displacement decomposition. We consider an element e where two reference surface coordinates are introduced as

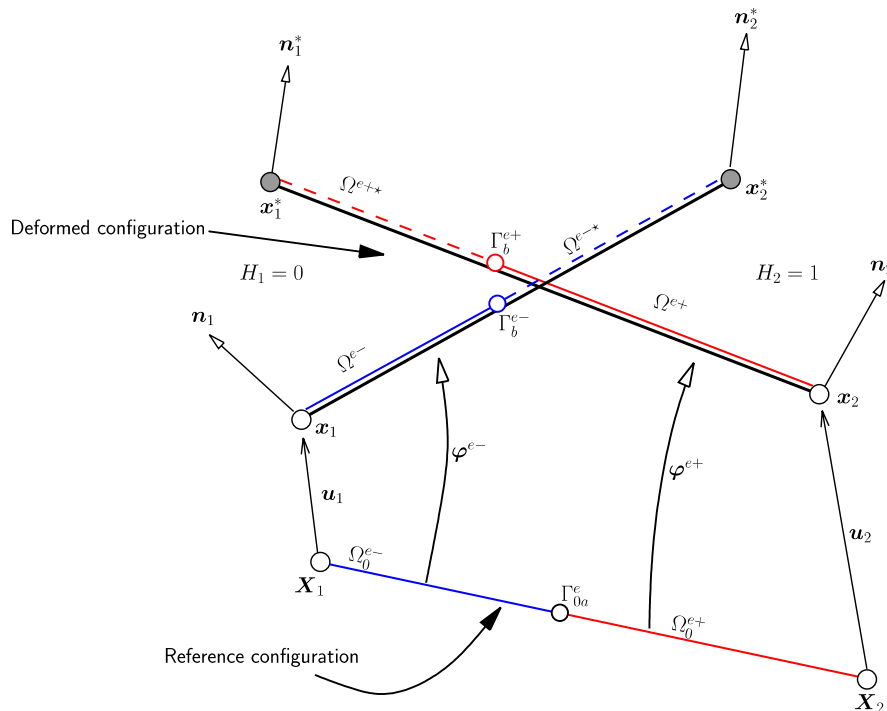


Fig. 2. Representation of a cracked beam as two superimposed elements ($\Omega^{e-\star} \cup \Omega^{e-}$ and $\Omega^{e+\star} \cup \Omega^{e+}$) using two distinct deformation maps (φ^- and φ^+). Note that the integration is performed only on part of each superimposed element (the energy corresponding to dashed lines is *not* accounted for).

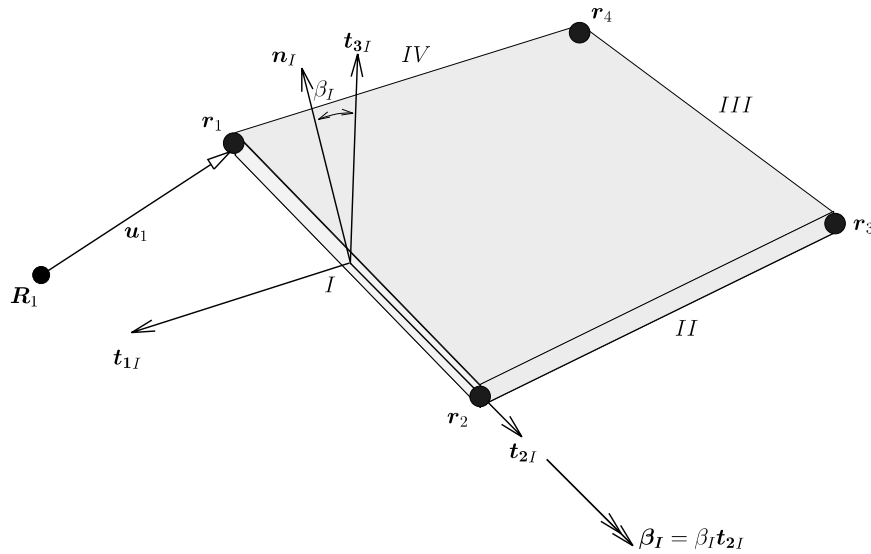


Fig. 3. Shell element based on discrete Kirchhoff-Love conditions. Directors (\mathbf{n}_I is represented) are interpolated at the mid-sides. For simplicity only the rotation of side I is shown.

$\boldsymbol{\theta} = \{\theta^1, \theta^2\}$ such that $\boldsymbol{\theta} \in [-1, 1]^2$ and a third coordinate identified as the signed distance to the reference surface, θ^3 . Using the notation \mathbf{r}^+ and \mathbf{r}^- for the mid-surface positions of the shell element in each of the parts $\Omega^{e-} \cup \Omega^{e-\star}$ and $\Omega^{e+} \cup \Omega^{e+\star}$, respectively, we can write \mathbf{r} as

$$\mathbf{r} = \begin{cases} \underbrace{\sum_{K=1}^4 (1 - H_K) N_K(\boldsymbol{\theta}) \mathbf{r}_K + \sum_{K=1}^4 H_K N_K(\boldsymbol{\theta}) \mathbf{r}_K^*}_{\mathbf{r}^+}, & f(\mathbf{X}) > 0, \\ \underbrace{\sum_{K=1}^4 H_K N_K(\boldsymbol{\theta}) \mathbf{r}_K + \sum_{K=1}^4 (1 - H_K) N_K(\boldsymbol{\theta}) \mathbf{r}_K^*}_{\mathbf{r}^-}, & f(\mathbf{X}) < 0, \end{cases} \quad (2)$$

where K is the corner node number for Ω^e and $N_K(\boldsymbol{\theta})$ represents the bilinear shape function of corner node K . For the spatial directors, the same type of interpolation follows, where use is made of two directors \mathbf{n}^+ and \mathbf{n}^- :

$$\mathbf{n} = \begin{cases} \underbrace{\sum_{L=1}^{IV} (1 - H_L) M_L(\boldsymbol{\theta}) \mathbf{n}_L + \sum_{L=1}^{IV} H_L M_L(\boldsymbol{\theta}) \mathbf{n}_L^*}_{\mathbf{n}^+}, & f(\mathbf{X}) > 0, \\ \underbrace{\sum_{L=1}^{IV} H_L M_L(\boldsymbol{\theta}) \mathbf{n}_L + \sum_{L=1}^{IV} (1 - H_L) M_L(\boldsymbol{\theta}) \mathbf{n}_L^*}_{\mathbf{n}^-}, & f(\mathbf{X}) < 0, \end{cases} \quad (3)$$

with L being the mid-side node number ($L = \text{I}, \dots, \text{IV}$) and $M_L(\boldsymbol{\theta})$ represents the mid-side shape function corresponding to node L . The shape functions $M_L(\boldsymbol{\theta})$ are given by (see also [8]):

$$M_L(\theta^1, \theta^2) = \frac{1}{4} + \frac{3}{8} (\theta^{2L})^2 [(\theta^2)^2 - (\theta^1)^2] + \frac{1}{2} \theta^{2L} \theta^2 + \frac{3}{8} (\theta^{1L})^2 [(\theta^1)^2 - (\theta^2)^2] + \frac{1}{2} \theta^{1L} \theta^1. \quad (4)$$

Note that, despite the apparent simplicity of the relations (2), the nodal directors \mathbf{n}_L and \mathbf{n}_L^* are functions of both \mathbf{r} and \mathbf{r}^* in (2), because of the Kirchhoff-Love conditions as will become apparent later. Using the decompositions (2), the position of a given point \mathbf{X} can be presented as a function of the sub-domain to which it belongs:

$$\mathbf{x} \equiv \boldsymbol{\varphi}(\mathbf{X}) = \begin{cases} \underbrace{\mathbf{r}^+(\boldsymbol{\theta}) + \theta^3 \mathbf{n}^+(\boldsymbol{\theta})}_{\mathbf{x}^+}, & f(\mathbf{X}) > 0, \\ \underbrace{\mathbf{r}^-(\boldsymbol{\theta}) + \theta^3 \mathbf{n}^-(\boldsymbol{\theta})}_{\mathbf{x}^-}, & f(\mathbf{X}) < 0. \end{cases} \quad (5)$$

In the following, we use the notation $(\bullet)_{,\alpha}$ to denote derivatives with respect to θ^α , $\alpha = 1, 2$ and analogously $(\bullet)_{,i}$ for θ^i ; $i = 1, 2, 3$ with (\bullet) being an arbitrary quantity.

Let s^{ij} represent the contravariant components of the Kirchhoff stress tensor (in the basis $\mathbf{x}_{,\alpha} \otimes \mathbf{x}_{,\beta}$) which are also the components of the second Piola-Kirchhoff stress tensor in the basis $\mathbf{X}_{,\alpha} \otimes \mathbf{X}_{,\beta}$. Then the weak form of equilibrium can be written, using a parent domain volume $\mathcal{V}^e = [-1, 1]^2 \times [-h/2, h/2]$ for each element, and using $\sqrt{G} = \mathbf{X}_{,1} \cdot (\mathbf{X}_{,2} \times \mathbf{X}_{,3})$, as

$$\sum_{e=1}^{Ne} \int_{V^e} s^{\alpha\beta} \mathbf{x}_{,\beta} \cdot \delta \mathbf{x}_{,\alpha} \sqrt{G} d\theta^1 d\theta^2 d\theta^3 = \delta W_E, \quad (6)$$

where δW_E is the virtual work performed by the external loading and cohesive forces (given in Section 4). The derivatives $(\bullet)_{,\alpha}$ follow from the derivatives of the shape functions $N_K(\boldsymbol{\theta})$ and $M_L(\boldsymbol{\theta})$, denoted as $N_{K,\alpha} = \frac{\partial N_K}{\partial \theta^\alpha}$ and $M_{L,\alpha} = \frac{\partial M_L}{\partial \theta^\alpha}$. The upper limit Ne is the total number of elements in a particular discretization.

Our formulation is based on the covariant components of the Cauchy–Green deformation tensor. If the covariant components of the material metric tensor are introduced as

$$G_{ij} = \mathbf{X}_{,i} \cdot \mathbf{X}_{,j}, \quad (7)$$

then the contravariant components of the material metric tensor are given by $[G^{ij}] = [G_{ij}]^{-1}$ and the Cauchy–Green tensor is obtained using the contravariant basis vectors $\mathbf{G}^i = G^{ij} \mathbf{X}_{,j}$:

$$\mathbf{C} = \underbrace{\mathbf{x}_{,i} \cdot \mathbf{x}_{,j}}_{C_{ij}} \mathbf{G}^i \otimes \mathbf{G}^j. \quad (8)$$

The Kirchhoff–Love conditions are imposed to \mathbf{C} as

$$C_{i3} = \delta_{i3}, \quad (9)$$

where δ_{ij} represent the identity tensor components. The above relation provides a constraint between \mathbf{r} and \mathbf{n} , which is enforced at the four mid-side nodes in each element (see also [8]). Specifically, referring to Fig. 4, we impose $C_{33} = 1$ in all mid-side nodes I–IV, $C_{13} = \delta_{13} = 0$ in nodes I and III and $C_{23} = \delta_{23} = 0$ in nodes II and IV. It is worth noting that the Kirchhoff–Love constraints remain satisfied if the element is cracked.

Using the procedure in [8], we can write the deformed normal vector at the mid-side node I as

$$\mathbf{n}_I = \mathbf{R}^* (\beta_I, \beta_I^*) \mathbf{R}(\mathbf{r}, \mathbf{r}^*) \mathbf{n}_{0I} \quad (10)$$

with \mathbf{R}^* being a rotation matrix corresponding to side I rotation and \mathbf{R} being the rotation of the material normal \mathbf{n}_{0I} due to deformation of the element. Further details concerning this procedure can be found in [8]. It is noted that the Rodrigues formula (e.g. [1]) can be particularized in the second rotation matrix \mathbf{R} (see [8]).

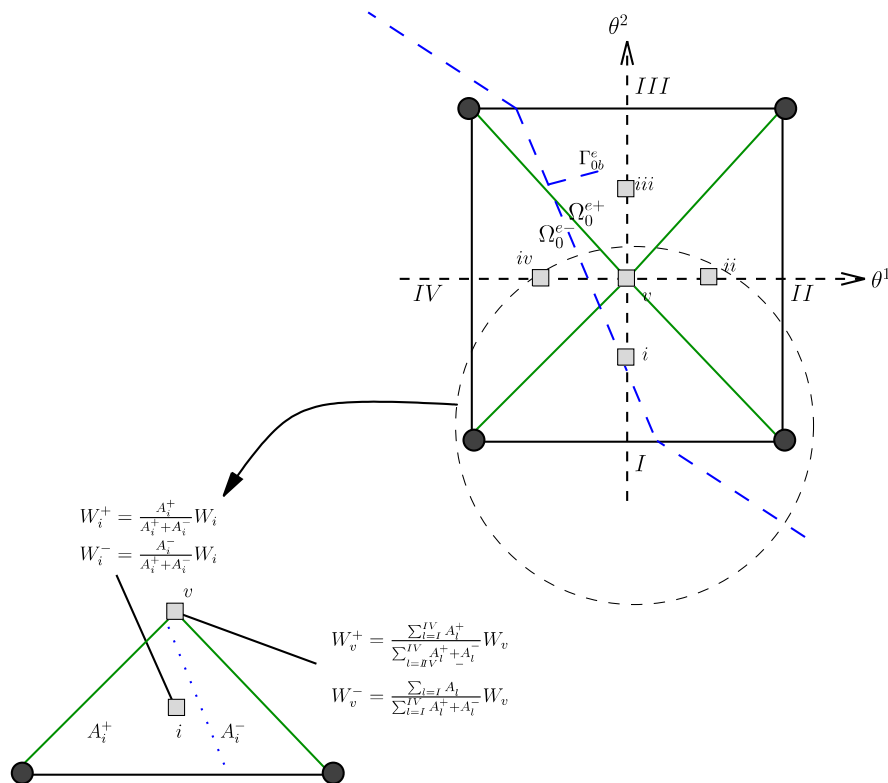


Fig. 4. Modified quadrature weights. A five point quadrature rule is employed (see [8]). For simplicity, only the cases of points i and v are depicted. Note that $A_i^+ + A_i^- = 1$ in the parent domain.

The first variation of $\mathbf{x}_{,\beta}$; $\delta\mathbf{x}_{,\beta}$, can be written, according to the corresponding sub-domain, as

$$\delta\mathbf{x}_{,\alpha}^+ = \sum_{K=1}^4 (1 - H_K) N_{K,\alpha} \delta\mathbf{r}_K + \sum_{K=1}^4 H_K N_{K,\alpha} \delta\mathbf{r}_K^* + \sum_{L=1}^{IV} (1 - H_L) M_L(\boldsymbol{\theta}) \delta\mathbf{n}_L(\delta\mathbf{x}_k, \delta\mathbf{x}_k^*, \delta\beta_l) + \sum_{L=1}^{IV} H_L M_L(\boldsymbol{\theta}) \delta\mathbf{n}_L^*(\delta\mathbf{x}_k, \delta\mathbf{x}_k^*, \delta\beta_l^*), \quad (11a)$$

$$\delta\mathbf{x}_{,\alpha}^- = \sum_{K=1}^4 H_K N_{K,\alpha} \delta\mathbf{r}_K + \sum_{K=1}^4 (1 - H_K) N_{K,\alpha} \delta\mathbf{r}_K^* + \sum_{L=1}^{IV} H_L M_L(\boldsymbol{\theta}) \delta\mathbf{n}_L(\delta\mathbf{x}_k, \delta\mathbf{x}_k^*, \delta\beta_l) + \sum_{L=1}^{IV} (1 - H_L) M_L(\boldsymbol{\theta}) \delta\mathbf{n}_L^*(\delta\mathbf{x}_k, \delta\mathbf{x}_k^*, \delta\beta_l^*), \quad (11b)$$

where the explicit dependence of \mathbf{n}_L and \mathbf{n}_L^* on \mathbf{x}_k , \mathbf{x}_k^* , β_l and β_l^* is apparent, with $k = 1, \dots, 4$ and $l = I, \dots, IV$ (note the use of lower case subscripts for these arguments).

The modified quadrature weights are represented in Fig. 4 and are calculated in the mid-surface parent domain $\boldsymbol{\theta} \in [-1, 1]^2$. We scale the weights so that the correct areas for each of the parts Ω_e^+ and Ω_e^- is obtained.

The first variation of δW_I , which is required for the calculation of the tangent matrix, is given by

$$\begin{aligned} d\delta W_I = & \sum_{e=1}^{Ne} \int_{V^e} \left\{ s^{\alpha\beta} [(\mathbf{d}\mathbf{r}_{,\alpha} + \theta^3 \mathbf{d}\mathbf{n}_{,\alpha}) \cdot (\delta\mathbf{r}_{,\beta} + \theta^3 \delta\mathbf{n}_{,\beta}) + (\mathbf{r}_{,\alpha} + \theta^3 \mathbf{n}_{,\alpha}) \cdot (\mathbf{d}\delta\mathbf{r}_{,\beta} + \theta^3 \mathbf{d}\delta\mathbf{n}_{,\beta})] \right. \\ & + 2\mathfrak{C}^{\alpha\beta\gamma\eta} [(\mathbf{r}_{,\alpha} + \theta^3 \mathbf{n}_{,\alpha}) \cdot (\delta\mathbf{r}_{,\beta} + \theta^3 \delta\mathbf{n}_{,\beta})][(\mathbf{r}_{,\gamma} + \theta^3 \mathbf{n}_{,\gamma}) \cdot (\mathbf{d}\mathbf{r}_{,\eta} + \theta^3 \mathbf{d}\mathbf{n}_{,\eta})] + \delta s^{\alpha\beta} (\mathbf{d}\mathbf{n} \cdot \mathbf{r}_{,\alpha} + \mathbf{n} \cdot \mathbf{d}\mathbf{r}_{,\alpha}) \\ & \left. + \delta s^{\alpha\beta} (\delta\mathbf{n} \cdot \mathbf{r}_{,\alpha} + \mathbf{n} \cdot \delta\mathbf{r}_{,\alpha}) + s^{\alpha\beta} (\mathbf{d}\delta\mathbf{n} \cdot \mathbf{r}_{,\alpha} + \mathbf{d}\mathbf{n} \cdot \delta\mathbf{r}_{,\alpha}) + s^{\alpha\beta} (\delta\mathbf{n} \cdot \mathbf{d}\mathbf{r}_{,\alpha} + \mathbf{n} \cdot \mathbf{d}\delta\mathbf{r}_{,\alpha}) \right\} \sqrt{G} d\theta^1 d\theta^2 d\theta^3 \end{aligned} \quad (12)$$

with $\mathfrak{C}^{\alpha\beta\gamma\eta}$ representing the contravariant components of the consistent modulus, to be introduced in the following section. The tangent stiffness matrix obtained from (12) is generally unsymmetric in the elasto-plastic case.

The interpretation as a XFEM element can be carried out very simply if we introduce the nodal sign as $s_K = 2H_K - 1$ and write the displacement as $\mathbf{u} = H\mathbf{u}^+ + (1 - H)\mathbf{u}^-$ with H denoting the step function. Then, it is possible to show that the traditional XFEM degrees of freedom are obtained by linear combination of the present method degrees of freedom. The proof has been given in [20].

3. Elastic–plastic algorithm

In our previous work [8], we used the contravariant components of the Kirchhoff stress tensor to establish the weak form of equilibrium equations for the shell model. To take advantage of the simplicity of our previous derivations, we retain the curvilinear coordinates in the inelastic range.

With that purpose, we use the large strain elasto-plastic formulation by Miehe [21] particularized for a Kirchhoff–Love shell model. In contrast with that work, we do not use a spectral decomposition of the Cauchy–Green tensor and opt to use Padé interpolants (see also [22] and [15]). Note that this corresponds to the *dual* formulation of elasto-plasticity [23] (in stress space) and is now a common procedure in many applications. For this reason, and because we are confined to *isotropic* constitutive laws, we only present the main results. The formulation follows the multiplicative decomposition of the deformation gradient \mathbf{F} , as in Lee [14], and employed with success in the seminal work of Simó and Ortiz [24]:

$$\mathbf{F} = \mathbf{F}^e \mathbf{F}^p. \quad (13)$$

We define the right Cauchy–Green tensors (elastic and plastic) accordingly

$$\begin{aligned} \mathbf{C}^e &= \mathbf{F}^{eT} \mathbf{F}^e, \\ \mathbf{C}^p &= \mathbf{F}^{pT} \mathbf{F}^p. \end{aligned}$$

Note that \mathbf{C}^p is also called the covariant plastic metric.

With this notation, we can introduce a generally unsymmetric tensor \mathbf{C}^E such as

$$\mathbf{C} = \mathbf{C}^E \mathbf{C}^p. \quad (14)$$

The elasto-plastic formulation based on decomposition (14) circumvents the explicit evolution for the plastic spin (and also the non-uniqueness aspect of Lee’s decomposition (13)). \mathbf{C}^E can be written as a function of \mathbf{C}^e according to

$$\mathbf{C}^E = \mathbf{F}^{p^{-1}} \mathbf{C}^e \mathbf{F}^p. \quad (15)$$

The formulation does not rely on the explicit identification of \mathbf{F}^e or \mathbf{F}^p and these quantities remain undetermined. Making use of a spectral decomposition of \mathbf{C}^e and relating it to \mathbf{C}^E , we make further progress by identifying that they possess analogous forms:

$$\mathbf{C}^e = \mathbf{N} \mathbf{E} \mathbf{N}^T, \quad (16)$$

with \mathbf{N} being a matrix containing, columnwise, the *unitary* eigenvectors of \mathbf{C}^e and $\mathbf{E} = \text{diag}[\lambda_i^2]$ where λ_i are the principal *elastic* stretches. Due to orthogonality of the eigenvectors, $\mathbf{N}^T = \mathbf{N}^{-1}$. Inserting (16) into (15), we obtain

$$\mathbf{C}^E = (\mathbf{F}^p \mathbf{N}) \mathbf{E} (\mathbf{F}^p \mathbf{N})^{-1}. \quad (17)$$

If we introduce $\mathbf{N}^E = \mathbf{F}^p \mathbf{N}$ then it is clear that \mathbf{C}^p can be expressed as

$$\mathbf{C}^p = \mathbf{N}^E \mathbf{N}^{E^T}. \quad (18)$$

A more concise decomposition of \mathbf{C}^E is obtained, identifying \mathbf{N}^E as the matrix of *right* eigenvectors of \mathbf{C}^E :

$$\mathbf{C}^E = \mathbf{N}^E \mathbf{E} \mathbf{N}^{E^{-1}}. \quad (19)$$

After decomposing \mathbf{C}^E according to (19), we can normalize the eigenvectors with Eq. (18).

Using (19), we can write the spectral decomposition of \mathbf{C} , as a counterpart of (16), keeping in mind that \mathbf{N}^E is not generally composed of unitary vectors (as is \mathbf{N}):

$$\mathbf{C} = \mathbf{N}^E \mathbf{E} \mathbf{N}^{E^T}. \quad (20)$$

These direct derivations are, however, purposeless if \mathbf{C}^p is obtained directly from \mathbf{F}^p (i.e. if \mathbf{F}^p is considered to be an historical variable). Let us introduce an isotropic strain energy density as a function of the state variables \mathbf{C} , which is a measure of total strain, \mathbf{C}^p which is a measure of plastic strain, and ξ which represents the set of remaining internal variables of state. The set $\{\mathbf{C}^p, \xi\}$ constitutes the internal variables. We use the usual notation ψ for the strain energy function:

$$\psi \equiv \psi(\mathbf{C}, \mathbf{C}^p, \xi). \quad (21)$$

The evolution laws of both \mathbf{C}^p and ξ are derived as to comply, ab initio, with the second law of thermodynamics, which can be written in the form of the Clausius–Planck inequality, in the absence of thermal terms

$$\mathcal{D}_{\text{int}} = \frac{1}{2} \mathbf{S} : \dot{\mathbf{C}} - \dot{\psi} \geq 0, \quad (22)$$

where \mathcal{D}_{int} is the internal dissipation term. Inserting the time-derivative of (21) into (22) it is possible to write

$$\mathcal{D}_{\text{int}} = \left(\frac{1}{2} \mathbf{S} - \frac{\partial \psi}{\partial \mathbf{C}} \right) : \dot{\mathbf{C}} - \mathbf{S}^p : \dot{\mathbf{C}}^p - \chi : \dot{\xi} \geq 0, \quad (23)$$

where $\mathbf{S}^p = \frac{\partial \psi}{\partial \mathbf{C}^p}$ and $\chi = \frac{\partial \psi}{\partial \xi}$. Using the fact that, in the absence of plastic evolution and “frozen” internal variable evolution (i.e. $\dot{\xi} = 0$) the constitutive law should still satisfy (23) and the accompanying process is non-dissipative ($\mathcal{D}_{\text{int}} = 0$), we are able to write $\mathbf{S} = 2 \frac{\partial \psi}{\partial \mathbf{C}}$ for this condition to hold for arbitrary $\dot{\mathbf{C}}$. Of course, if one of the previous conditions for the internal variable evolution does not hold, it is possible to have a distinct value for \mathbf{S} , but this situation is not considered in our work (see also [25]). Note that $\dot{\mathbf{C}}^p = 0$ does *not* generally imply that $\dot{\xi} = 0$, but this is assumed to hold. The evolution laws are obtained from a “potential” of dissipation, which is denoted as

$$\mathcal{F} \equiv \mathcal{F}(\mathbf{C}^p, \xi; \mathbf{S}^p, \chi) \quad (24)$$

from which we postulate that

$$\begin{aligned} \dot{\mathbf{C}}^p &= \dot{\alpha} \frac{\partial \mathcal{F}}{\partial \mathbf{S}^p}, \\ \dot{\xi} &= \dot{\alpha} \frac{\partial \mathcal{F}}{\partial \chi}, \end{aligned}$$

where $\dot{\alpha} \geq 0$ is a plastic parameter (also called plastic multiplier in the associative case).

Let us introduce the elastic part of the strain energy function (the strain energy function can be decomposed into elastic and plastic parts, e.g. [23]) as a function of the principal elastic stretches: $\psi^e \equiv \psi^e(\lambda_i)$ with $i = 1, 2, 3$. If we introduce the principal *elastic* Hencky strain components as $\varepsilon_i = \ln \lambda_i$, and the principal Kirchhoff stress components as $\tau_i = \frac{\partial \psi^e}{\partial \varepsilon_i}$, it is possible to express, under coaxiality conditions, the second Piola–Kirchhoff stress tensor as

$$\mathbf{S} = \mathbf{N}^{E^{-T}} \mathbf{S}_D \mathbf{N}^{E^{-1}} = s^{\alpha\beta} \mathbf{X}_{,\alpha} \otimes \mathbf{X}_{,\beta}, \quad (25)$$

with $\mathbf{S}_D = \text{diag}[\frac{\tau_i}{\lambda_i^2}]$. A conjugate force to the plastic metric \mathbf{C}^p is \mathbf{S}^p , the plastic force, which can be written as

$$\mathbf{S}^p = \frac{\partial \psi^e}{\partial \mathbf{C}^p} = \frac{1}{2} \mathbf{C}^{p^{-1}} \mathbf{C} \mathbf{S}, \quad (26)$$

where use was made of the chain rule and symmetry of \mathbf{C}^p , \mathbf{C} and \mathbf{S} and the symmetry of the result:

$$\frac{\partial \psi}{\partial \mathbf{C}^p} = \frac{\partial \psi}{\partial \mathbf{C}} : \frac{\partial \mathbf{C}}{\partial \mathbf{C}^p} = \frac{1}{2} \mathbf{S} \mathbf{C}^E = \frac{1}{2} \mathbf{C}^{E^T} \mathbf{S}. \quad (27)$$

The term $\mathbf{C}\mathbf{S}$ in (26) is the so-called mixed-variant stress tensor [21,25], and is here denoted as $\mathbf{\Sigma}$. This tensor is generally unsymmetric.

Finally, the flow law can be written as

$$\dot{\mathbf{C}}^p = 2\alpha \frac{\partial \mathcal{F}}{\partial \mathbf{\Sigma}} \mathbf{C}^p \quad (28)$$

and the elastic law is given by

$$\mathbf{\Sigma} = \kappa \operatorname{tr} \boldsymbol{\varepsilon} \mathbf{I} + \mu \operatorname{dev} \boldsymbol{\varepsilon}, \quad (29)$$

with

$$2\boldsymbol{\varepsilon} = \ln \mathbf{C}^E.$$

Let us now integrate the flow law (28) using the exponential mapping, by introducing two time steps t_n and t_{n+1} , a time increment denoted $\Delta t = t_{n+1} - t_n$, and the variation of the plastic multiplier between these two instants ($\Delta \alpha$):

$$\mathbf{C}_{n+1}^E = \mathbf{C}_{n\star}^E \exp \left[-2\Delta \alpha \frac{\partial \mathcal{F}}{\partial \mathbf{\Sigma}} \right], \quad (30)$$

where $\mathbf{C}_{n\star}^E$ is given by

$$\mathbf{C}_{n\star}^E = \mathbf{C}_{n+1} \mathbf{C}_n^{p-1} \quad (31)$$

or, making use of the notation $\boldsymbol{\varepsilon}_{n+1}$ and $\boldsymbol{\varepsilon}_{n\star}$:

$$\boldsymbol{\varepsilon}_{n+1} = \boldsymbol{\varepsilon}_{n\star} - \Delta \alpha \frac{\partial \mathcal{F}}{\partial \mathbf{\Sigma}}. \quad (32)$$

Note that the finite strain consistent modulus can be written as a function of a “small strain” modulus \mathbb{C} using indicial notation:

$$\mathbb{C}_{ijkl} = \frac{\partial S_{ij}}{\partial C_{kl}^E} = C_{ir}^{-1} \mathbb{C}_{rjpk} \frac{\partial \varepsilon_{pq}}{\partial C_{kv}^E} C_{lv}^{p-1} - C_{ik}^{-1} C_{lr}^{-1} \Sigma_{rj}. \quad (33)$$

With (33) we can write the classical relation between the second Piola–Kirchhoff stress and the Green–Lagrange strain $\mathbf{E}_2 = \frac{1}{2} \mathbf{C} - \frac{1}{2} \mathbf{I}$ as $\dot{\mathbf{S}} = 2\mathbb{C} : \dot{\mathbf{E}}_2$.

The small strain analogy of (32) allows us to use a small strain elasto-plastic code, adequately modified to deal with unsymmetric stress and strain tensors. It is interesting to note that approximations to logarithms and exponentials can be employed, as these are found to be sufficient in metal plasticity, even for considerably large strains [22,15]. The algorithm in Table 1 shows the adopted procedure. We use first order approximations for the exponential and second order for the logarithm functions:

Table 1

The return mapping in the material setting; encapsulation of the small strain case

Make $\mathbf{C}_0^p = \mathbf{I}$ (and therefore $\mathbf{C}_0^{p-1} = \mathbf{I}$) and $\xi_0 = \mathbf{0}$ for all quadrature points

For each quadrature point at time-step n , perform the following calculations

- (1) Using the current position field \mathbf{x} calculate $\mathbf{C}_{n+1} = (\mathbf{x}_{,\alpha} \cdot \mathbf{x}_{,\beta}) \mathbf{G}^\alpha \otimes \mathbf{G}^\beta$ with $\mathbf{G}^\alpha = G^{\alpha\beta} \mathbf{X}_{,\beta}$ and $[G^{\alpha\beta}] = [\mathbf{X}_{,\alpha} \cdot \mathbf{X}_{,\beta}]^{-1}$
- (2) Calculate the trial of the elastic measure $\mathbf{C}_{n\star}^E = \mathbf{C}_{n+1} \mathbf{C}_n^{p-1}$
- (3) Use a second order Padé approximation to calculate $\boldsymbol{\varepsilon}_{n\star} = \frac{1}{2} \ln \mathbf{C}_{n\star}^E$
- (4) Using a *modified* (unsymmetric) small strain return-mapping algorithm, update ξ_n and calculate $\boldsymbol{\varepsilon}_{n+1} \Delta \alpha$, $\mathbf{\Sigma}$ and the small strain consistent modulus \mathbb{C}
- (5) Calculate the new plastic metric inverse as $\mathbf{C}_{n+1}^{p-1} = \mathbf{C}_{n+1}^{-1} \exp[2\boldsymbol{\varepsilon}_{n+1}]$ using a first order Padé approximation for the exponential function
- (6) Calculate the contravariant components of the stress as

$$s^{\alpha\beta} = \mathbf{G}^\alpha \cdot (\mathbf{C}^{-1} \mathbf{\Sigma} \mathbf{G}^\beta)$$

and the contravariant components of the tangent modulus as

$$\mathbb{C}^{\alpha\beta\gamma\delta} = G^{\alpha i} G^{\beta j} G^{\gamma k} G^{\delta l} \mathbb{C}_{ijkl}$$

with $G^{\alpha i} = \mathbf{G}^\alpha \cdot \mathbf{e}_i$ for any $i = 1, 2, 3$ and $\alpha = 1, 2$

$$\boldsymbol{\varepsilon} \cong \boldsymbol{\varepsilon}^1 = \boldsymbol{\varepsilon}^0 \left(\mathbf{I} - \frac{1}{3} \boldsymbol{\varepsilon}^0 \boldsymbol{\varepsilon}^0 \right)^{-1}, \quad (34a)$$

with

$$\boldsymbol{\varepsilon}^0 = (\mathbf{C}^E - \mathbf{I})(\mathbf{C}^E + \mathbf{I})^{-1} \quad (34b)$$

and

$$\mathbf{C}^E \cong (\mathbf{I} - \boldsymbol{\varepsilon})^{-1}(\mathbf{I} + \boldsymbol{\varepsilon}). \quad (34c)$$

The derivative $\frac{\partial \varepsilon_{pq}}{\partial C_{kv}^E}$ in (33) can use the first Padé approximation (34c) as the final \mathbf{C}^E is employed, which for metal plasticity is sufficiently close to the unitary matrix [22,15]. In this case

$$\frac{\partial \varepsilon_{pq}}{\partial C_{kv}^E} \cong \frac{\partial \varepsilon_{pq}^0}{\partial C_{kv}^E} = (\delta_{pk} - \varepsilon_{pk}^0)(\mathbf{I} + \mathbf{C}^E)_{vq}^{-1}.$$

The reason for using distinct orders of approximation in (34a) and (34c) is that the *trial* elastic strains can be substantially larger than the corrected elastic strains in metal plasticity.

In our present application, we employ J_2 associative plasticity, where the dissipation potential \mathcal{F} coincides with the yield function (see also [25]).

4. Cohesive law

We make use of a combination of a stability criterion (as a fracture indicator) and maximum principal strains (to predict the crack path) which was found to be convenient for fracture initiation and propagation [26]. For a KL constrained medium, the stability condition should take into account the KL constraints *and* the compatibility conditions (resulting in a set of non-simple constraints see, e.g. [19]).

The virtual work of the cohesive forces is included in the term δW_E in the right hand side of Eq. (6). The force introduced here corresponds to the resistance to opening, which is a function of the opening displacement itself. As this type of dissipation mechanism occurs in a set of measure zero, part of the energy dissipated in the continuum is transferred to the cohesive law (see, e.g. [26]). The opening displacement can be written as a function of the mid-surface position in both sides of the crack *and* the director in both sides of the cracked, for each cracked element. We denote the surface opening by Δu , which can be expressed as (see Fig. 5):

$$\Delta u = \Delta \mathbf{u} \cdot \mathbf{m}, \quad (35)$$

where $\Delta \mathbf{u}$ is defined according to

$$\Delta \mathbf{u} = \Delta \mathbf{r} + \theta^3 \Delta \mathbf{n} = \sum_{K=1}^4 (1 - 2H_K)(\mathbf{r}_K - \mathbf{r}_K^*)N_K(\boldsymbol{\theta}^*) + \theta^3 \sum_{L=1}^{IV} (1 - 2H_L)(\mathbf{n}_L - \mathbf{n}_L^*)M_L(\boldsymbol{\theta}^*), \quad (36)$$

where $\Delta \mathbf{r}$ is the mid-surface displacement jump and $\Delta \mathbf{n}$ is the director field jump. These are evaluated at the crack surface $\mathbf{X}(\boldsymbol{\theta}^*) \in \Gamma_{0b}$.

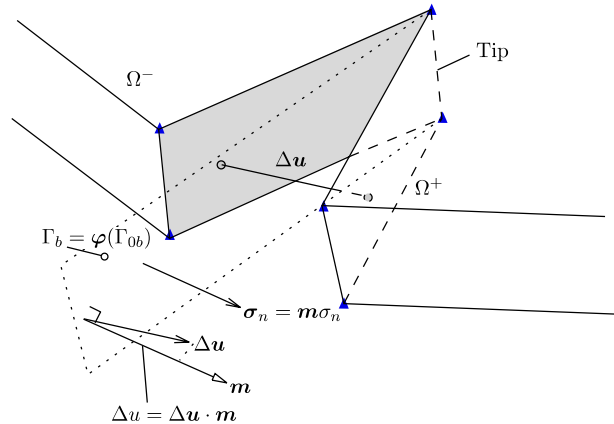


Fig. 5. Cohesive forces arising from the crack surface separation.

If we denote the part of δW_E corresponding to the cohesive virtual work as δW_E^c , then we can write it using the Kirchhoff stress value σ_n as

$$\delta W_E^c = - \int_{\Gamma_{Ob}} \sigma_n \delta \Delta u dA = - \int_{\Gamma_{Ob}} \boldsymbol{\sigma}_n \cdot \delta \Delta \mathbf{u} dA, \quad (37)$$

where A represents the area of Γ_{Ob}^c .

The first variation of δW_E^c is required for the application of the Newton method. It can be written as

$$d\delta W_E^c = - \int_{\Gamma_{Ob}} d\Delta \mathbf{u}^T \mathbf{K} \delta \Delta \mathbf{u} dA, \quad (38)$$

with

$$\mathbf{K} = \frac{\partial \sigma_n}{\partial \Delta u} \mathbf{m} \otimes \mathbf{m}. \quad (39)$$

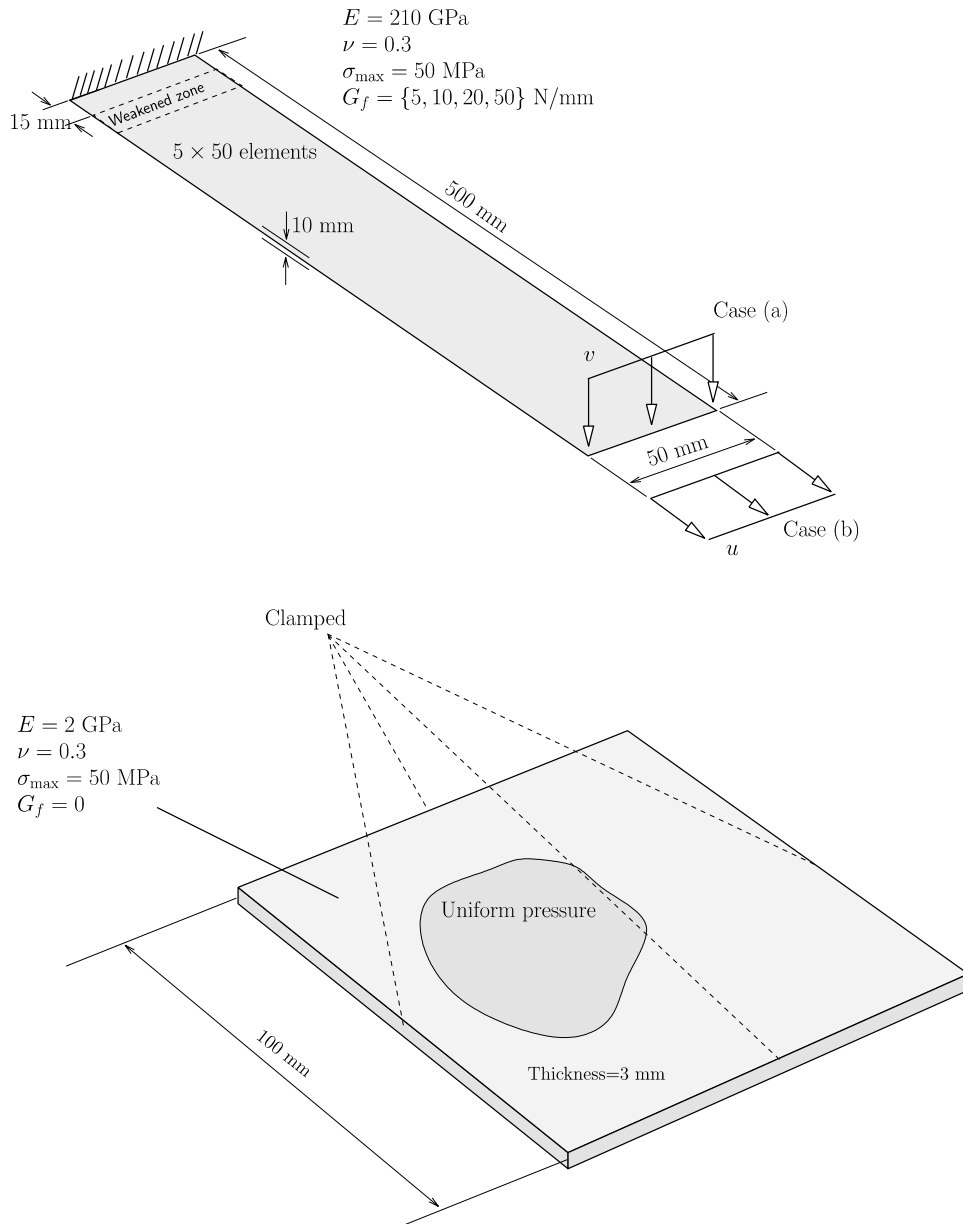


Fig. 6. Geometry and relevant data for the problems of a beam and a plate under pressure.

In the studies reported here, the particular constitutive model for the cohesive zone is given by (see also [27]):

$$\sigma_n = \frac{\sigma_{\max}}{\epsilon} \exp\left(-\frac{\sigma_{\max}}{G_f} \epsilon\right) \Delta u, \quad (40)$$

where σ_{\max} is the maximum cohesive stress, G_f is the fracture (surface) energy and $\epsilon = \max_{\text{history}} |\Delta u|$ denotes an internal variable. A penalty term is employed to attenuate crack face inter-penetration [27]. The Newton–Cotes formula is used in the quadrature of the cohesive terms, with four points identified with triangles in Fig. 5.

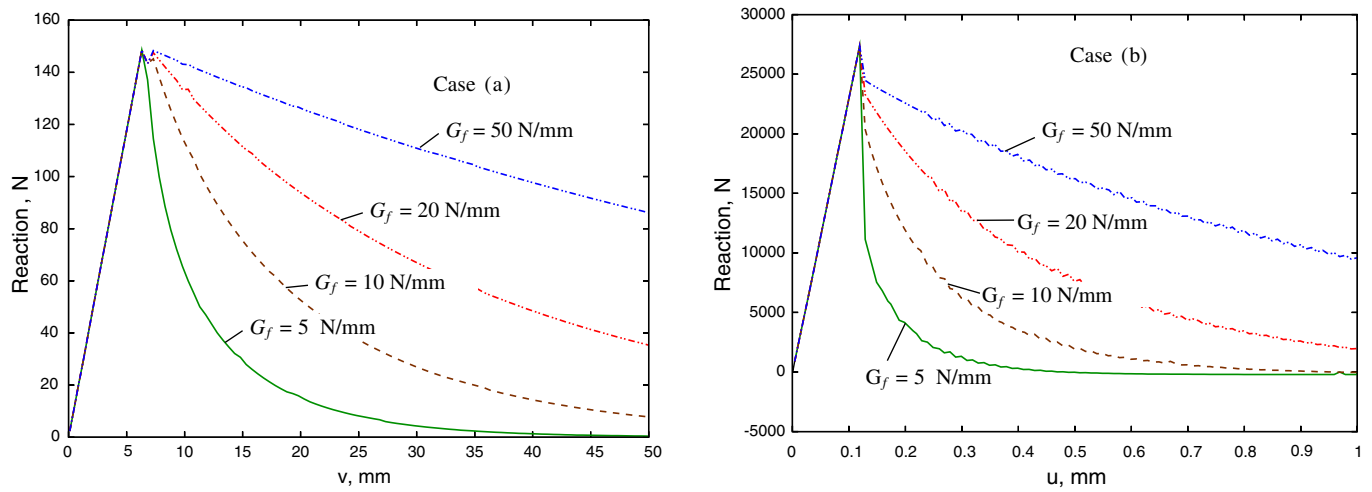


Fig. 7. Displacement-reaction results for the beam: cases (a) and (b) for several values of G_f .

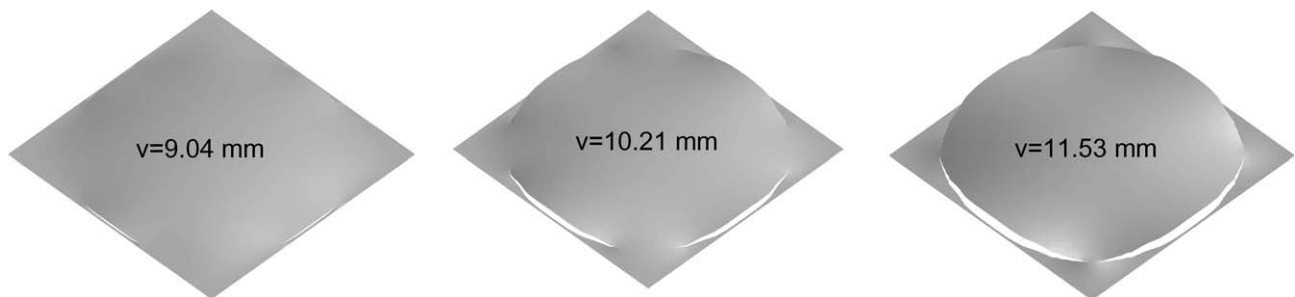


Fig. 8. Sequence of deformed (not magnified) configurations of the clamped plate, for increasingly higher transverse displacements.

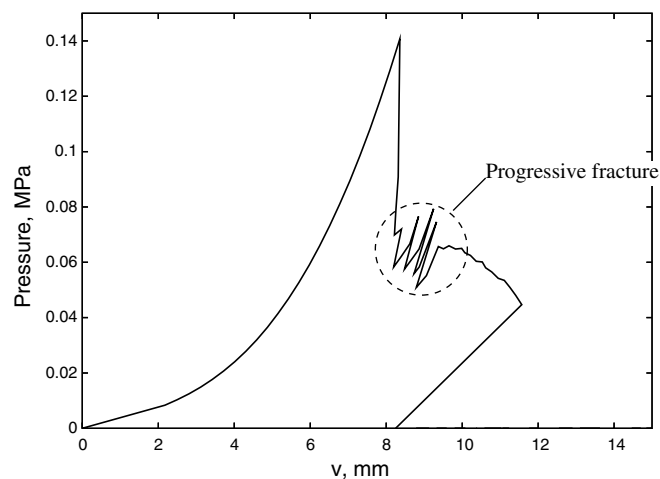


Fig. 9. Load-displacement results the clamped plate.

5. Numerical examples

The following numerical examples were run in the software SIMPLAS, created by the first author of this paper. A Post-script 3D post-processing software was also created by the same author. It was tested recently [7] using a non-linear EAS/XFEM variant of the Irons-Ahmad [28] shell element. The solution method is the residual-based damped Newton method (see also [29]) with arc-length continuation method.

5.1. Beam and plate brittle fracture

These two tests allow a simple assessment of the formulation and implementation, and in particular the inspection of locking between the crack faces, as it occurs in the context of certain embedded crack techniques, see [30]. They also provide an opportunity to test the cohesive law implementation. A noteworthy aspect of our implementation is that we can deactivate certain displacement components at the crack reference line ($\Delta r_i = 0$ for a given $i = 1, \dots, 3$), and therefore reproduce plastic hinges and other types of post-failure behavior. The beam and plate geometry and relevant properties are given in Fig. 6. The beam bending problem (corresponding to the case (a) in Fig. 6) is solved by constraining the relative displacement at the crack location in the lower cohesive line and allowing rotation using this line as axis.

For the beam problem, the reaction results are shown in Fig. 7. It can be seen that no spurious locking occurs, and this contrasts with un-modified versions of the embedded discontinuity method applied to plates [31].

For the plate, a regular mesh containing 80×80 elements is employed. The purpose is to verify what occurs in the absence of cohesive forces and plasticity. In that case, oscillations occur after each subset of elements crack. A sequence of deformed meshes is shown in Fig. 8. The corresponding central point displacement is also shown. The pressure versus displacement results are shown in Fig. 9. The effect of the discretization is apparent in this figure, with the oscillations in the pressure being induced by the sequential propagation through the elements.

5.2. Fracture of a hexcan

This problem was studied in Ref. [32] both experimentally and numerically. A hexagonal-base can, made of stainless steel type 316 is subjected to internal pressure up to fracture. From the test set of Ref. [32], we employ the specimen ST103I. The fracture stress is 1 GPa. The relevant data for this test is briefly described in Fig. 10.

As can be seen, the crack propagates along the corners of the Hexcan, a fact that was observed experimentally (Fig. 11).

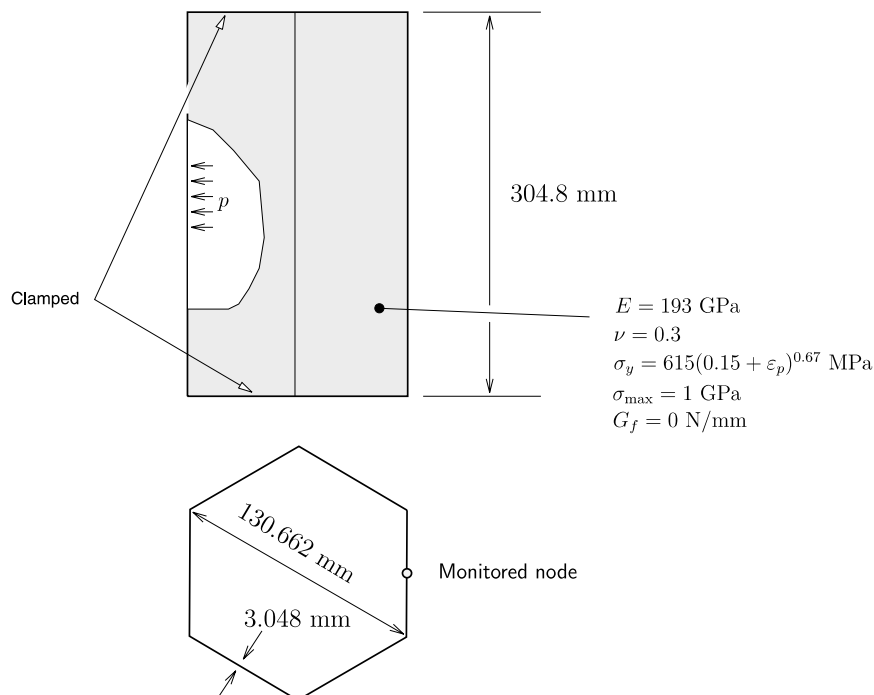


Fig. 10. Hexcan geometry and relevant properties.

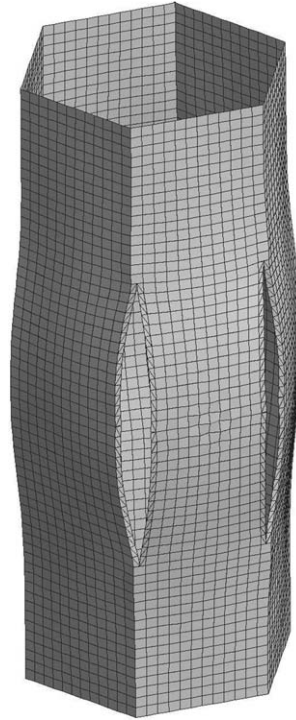


Fig. 11. Hexcan deformed mesh for a pressure of $p = 11.85$ MPa.

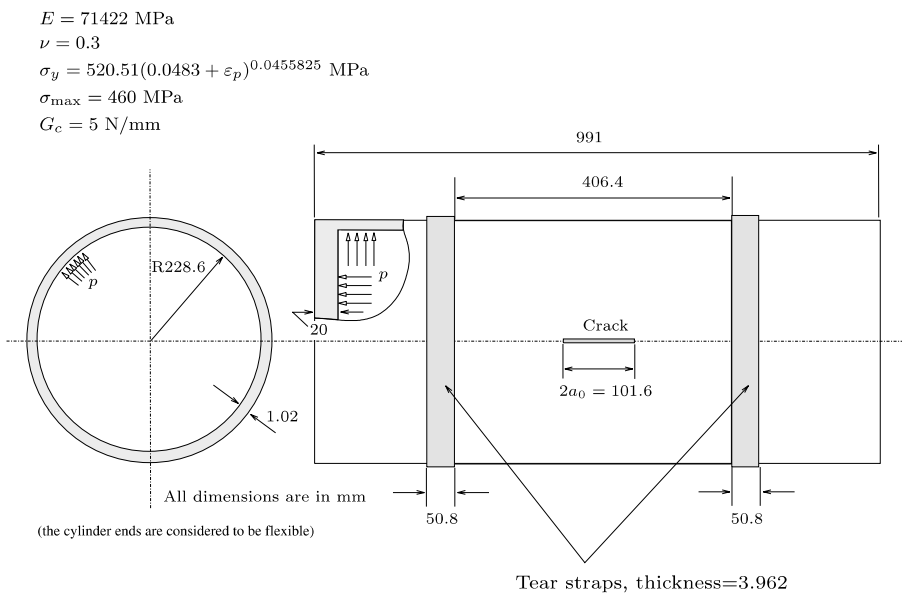


Fig. 12. Relevant data for the pressurized shell problem, see also Refs. [33,7]. Note the modified cylinder ends wall thickness.

5.3. Pressurized cylindrical shell with top and bottom ends

This example deals with the analysis of crack propagation in a pressurized cylinder and is based on the tests carried out by Keesecker et al. [33]. It was previously analysed using enhanced strain/XFEM elements in Ref. [7].

The cylinder is reinforced with two tear straps whose purpose is to induce “flapping”, i.e. to induce crack turning near these tear straps. If the purpose is fulfilled, axially propagating cracks are arrested.

Fig. 12 shows the reference configuration of the shell and the relevant properties. The hardening law is given by the relation $\sigma_y = 520.51(0.0483 + \varepsilon_p)^{0.0455825}$ where σ_y is the yield stress and ε_p is the effective plastic strain.

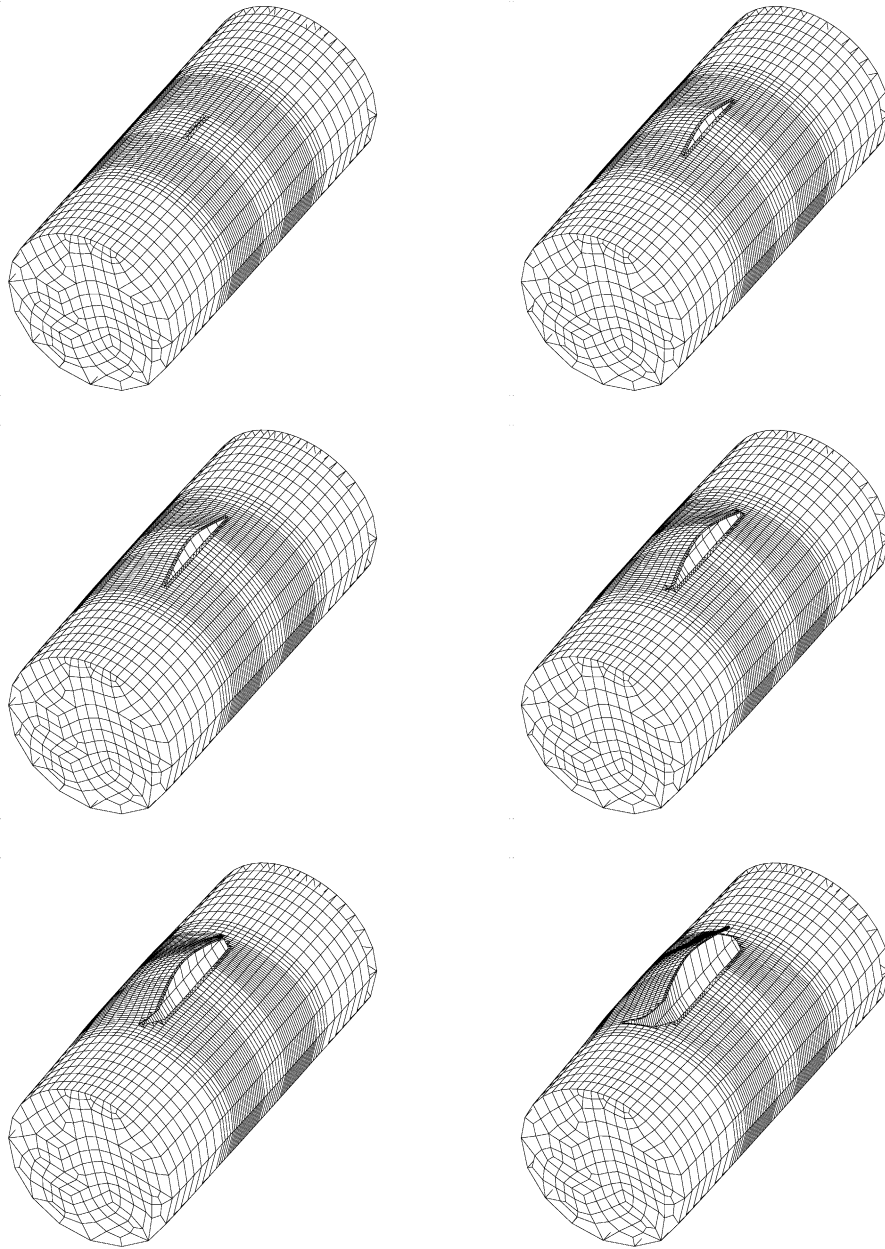


Fig. 13. Several steps in the flapping of a closed pressurized cylinder (*not magnified*). Note that the inner part of the cylinder is increasingly visible.

In [33], the CTOA (crack tip opening angle) criterion was used, with a critical value of 5° and in [7] the Rankine criterion was employed. To model the effect of the shell (pressurized) ends, in [7] multi-point constraints were employed. These are not required in the present context, because we can explicitly model the shell ends with our new shell element introduced in [8]. We use a end-wall thickness of 20 mm, as depicted in Fig. 12.

A sequence of deformed meshes is presented in Fig. 13. The bulging effect occurs during the self-similar stage of the analysis, and had a specific study in Ref. [34]. The growth of the crack is quite similar to that observed experimentally.

The effective plastic strain contour plot is shown in Fig. 14. It can be observed that the effective plastic strain values are rather low, but this is caused by elastic unloading after the crack formation.

The pressure-crack advance results are compared with the ones in Ref. [33] in Fig. 15.

5.4. Tearing of a plate by out-of-plane loading

This example is taken from Ref. [35] where an elasto-plastic plate is torn by the action of transverse point loading. The relevant data is presented in Fig. 16. We employ a 1722 element mesh, with a refinement in the center line. The final step

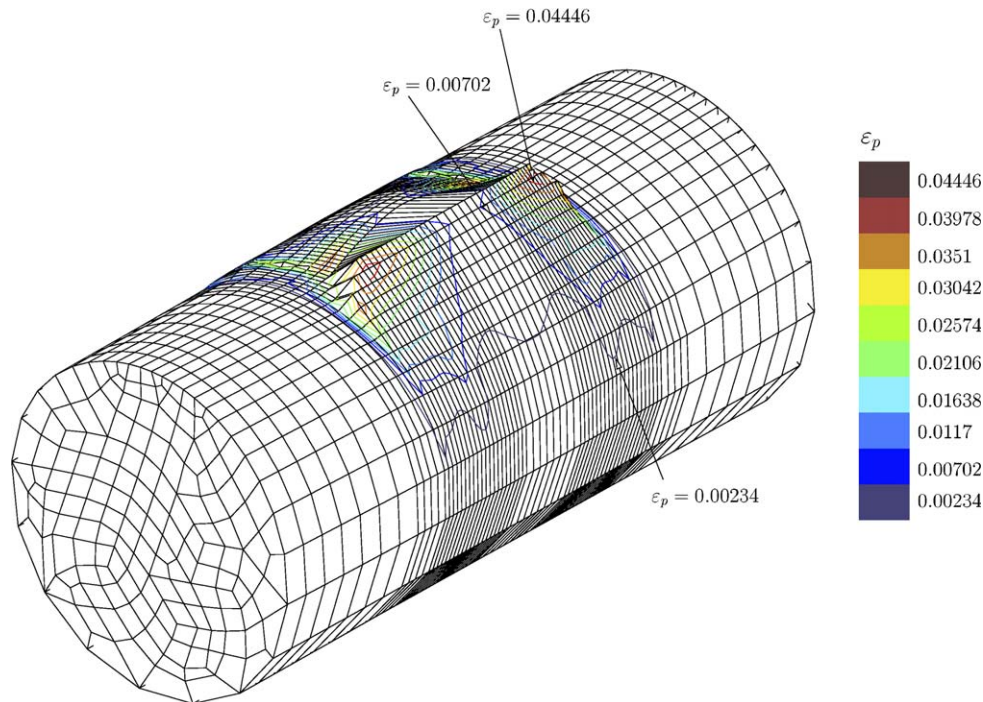


Fig. 14. Effective (averaged along the thickness) plastic strain contour plot.

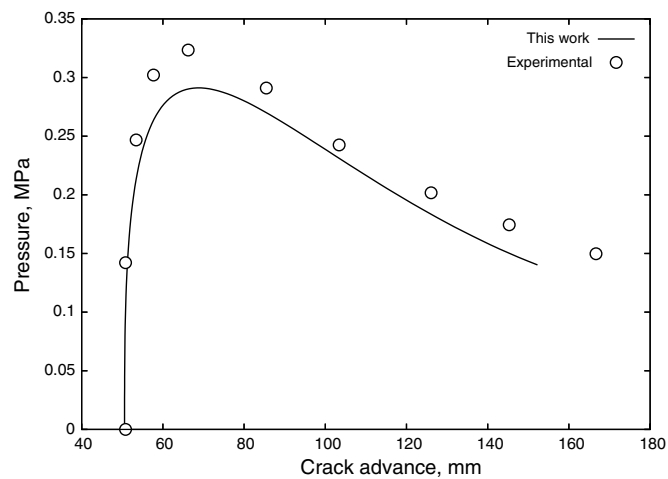


Fig. 15. Pressure-crack advance results for the pressurized cylinder.

during the deformation process is shown in Fig. 17 and corresponds to a tip displacement of 65.87 mm for a load of $2F = 1650$ N. The effective plastic strain contour plot, corresponding to an average along the thickness, are shown in Fig. 18. The load versus tip displacement curve is shown in Fig. 19 and reasonably agrees with the experimental results in the aforementioned reference.

6. Conclusions

We have developed an alternative technique to our previous developments concerning fracture in plates and shells. We proposed a modified enrichment, a technique to retain the same quadrature points and avoid the mapping of historical variables, and a fundamentally different finite element technology. We also showed an extension to finite plastic strains of the previous elasticity-only shell element formulated in curvilinear coordinates.

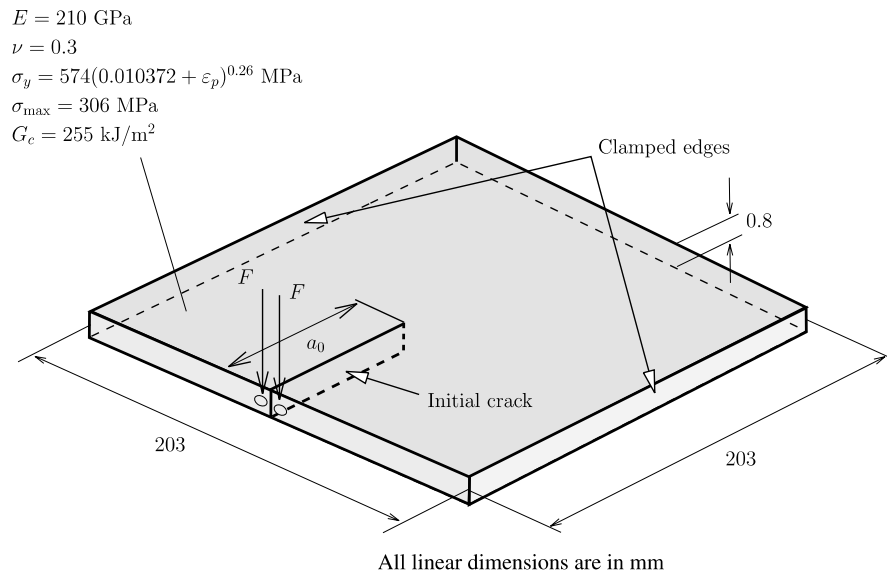


Fig. 16. The geometry, boundary conditions and relevant material properties for the plate problem (see also Ref. [35]). We employ $a_0 = 40 \text{ mm}$.

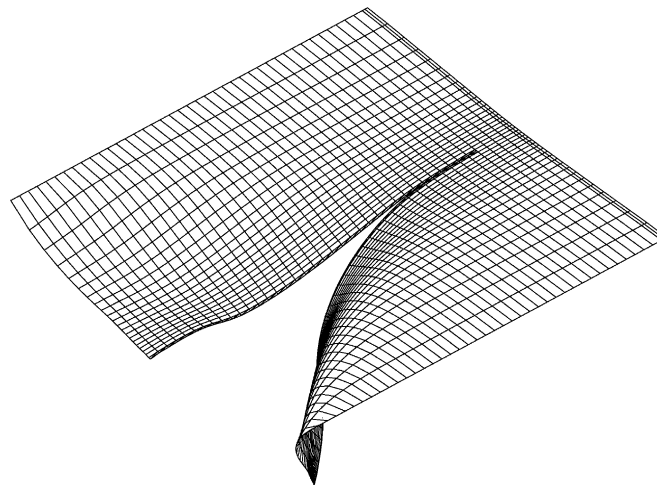


Fig. 17. Tearing of a plate: final deformed mesh for a load magnitude of $2F = 1650 \text{ N}$.

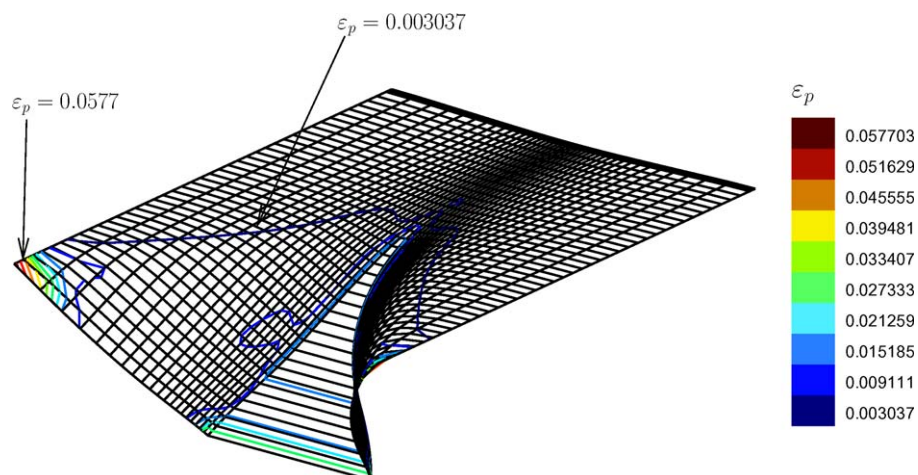


Fig. 18. Tearing of a plate: effective plastic strain contour plot.

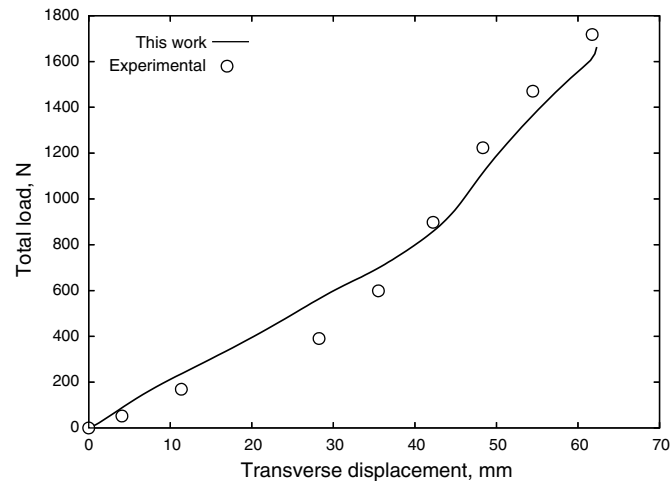


Fig. 19. Tearing of a plate: load–deflection curve (see also [35]).

Acknowledgement

The support of the Office of Naval Research and the Army Research Office is gratefully acknowledged.

References

- [1] J.H. Argyris, An excursion into large rotations, *Comput. Methods Appl. Mech. Engrg.* 32 (1982) 85–155.
- [2] J.C. Simo, D.D. Fox, On a stress resultant geometrically exact shell model. Part I: Formulation and optimal parametrization, *Comput. Methods Appl. Mech. Engrg.* 72 (1989) 267–304.
- [3] J.C. Simo, D.D. Fox, M.S. Rifai, On a stress resultant geometrically exact shell model. Part II: The linear theory; computational aspects, *Comput. Methods Appl. Mech. Engrg.* 73 (1989) 53–92.
- [4] N. Stander, A. Matzenmiller, E. Ramm, An assessment of assumed strain methods in finite rotation shell analysis, *Engrg. Comput.* 6 (1989) 58–65.
- [5] N. Buechter, E. Ramm, Shell theory versus degeneration—a comparison in large rotation finite element analysis, *Int. J. Numer. Methods Engrg.* 34 (1992) 39–59.
- [6] M. Bischoff, E. Ramm, Shear deformable shell elements for large strains and rotations, *Int. J. Numer. Methods Engrg.* 40 (1997) 4427–4449.
- [7] P.M.A. Areias, T. Belytschko, Non-linear analysis of shells with arbitrary evolving cracks using XFEM, *Int. J. Numer. Methods Engrg.* 62 (2005) 384–415.
- [8] P.M.A. Areias, J.-H. Song, T. Belytschko, A finite-strain quadrilateral shell element based on discrete Kirchhoff–Love constraints, *Int. J. Numer. Methods Engrg.* 64 (2005) 1166–1206.
- [9] A. Hansbo, P. Hansbo, A finite element method for the simulation of strong and weak discontinuities in solid mechanics, *Comput. Methods Appl. Mech. Engrg.* 193 (2004) 3523–3540.
- [10] J. Merghem, E. Kuhl, P. Steinmann, A finite element method for the computational modelling of cohesive cracks, *Int. J. Numer. Methods Engrg.* 63 (2005) 276–289.
- [11] J. Dolbow, N. Moës, T. Belytschko, Modeling fracture in Mindlin–Reissner plates with the extended finite element method, *Int. J. Solids Struct.* 37 (2000) 7161–7183.
- [12] F. Cirak, M. Ortiz, A. Pandolfi, A cohesive approach to thin-shell fracture and fragmentation, *Comput. Methods Appl. Mech. Engrg.* 194 (2005) 2604–2618.
- [13] Y.-W. Lee, J.C. Woertz, T. Wierzbicki, Fracture prediction of thin plates under hemi-spherical punch with calibration and experimental verification, *Int. J. Mech. Sci.* 46 (2004) 751–781.
- [14] E.H. Lee, Elasto-plastic deformation at finite strains, *ASME J. Appl. Mech.* 36 (1969) 1–6.
- [15] H. Baaser, The Padé-approximation for matrix exponentials applied to an integration algorithm preserving plastic incompressibility, *Computat. Mech.* 34 (2004) 237–245.
- [16] N. Moës, J. Dolbow, T. Belytschko, A finite element method for crack growth without remeshing, *Int. J. Numer. Methods Engrg.* 46 (1999) 131–150.
- [17] T. Belytschko, T. Black, Elastic crack growth in finite elements with minimal remeshing, *Int. J. Numer. Methods Engrg.* 45 (1999) 601–620.
- [18] T. Belytschko, N. Moës, S. Usui, C. Parimi, Arbitrary discontinuities in finite elements, *Int. J. Numer. Methods Engrg.* 50 (2001) 993–1013.
- [19] S.S. Antman, R.S. Marlow, Material constraints, Lagrange multipliers, and compatibility. Applications to rod and shell theories, *Arch. Rat. Mech. Anal.* 116 (1991) 257–299.
- [20] P. Areias, T. Belytschko, A comment on the article “A finite element method for simulation of strong and weak discontinuities in solid mechanics” by A. Hansbo and P. Hansbo [*Comput. Methods Appl. Mech. Engrg.* 193 (2004)], *Comput. Methods Appl. Mech. Engrg.* 193 (2004) 3523–3540.
- [21] C. Miehe, A constitutive frame of elastoplasticity at large strains based on the notion of a plastic metric, *Int. J. Solids Struct.* 35 (30) (1998) 3859–3897.
- [22] M. Brunig, Large strain elasto-plastic theory and nonlinear finite element analysis based on metric transformation tensors, *Computat. Mech.* 24 (1999) 187–196.
- [23] W. Han, B.D. Reddy, *Plasticity. Mathematical theory and numerical analysis* Interdisciplinary Applied Mathematics, vol. 9, Springer, 1999.

- [24] J.C. Simó, M. Ortiz, A unified approach to finite deformation elastoplastic analysis based on the use of hyperelastic constitutive equations, *Comput. Methods Appl. Mech. Engrg.* 49 (1985) 221–245.
- [25] P.M.A. Areias, J.M.A. César de Sá, C.A. Conceição António, A gradient model for finite strain elastoplasticity coupled with damage, *Finite Elem. Anal. Des.* 39 (2003) 1191–1235.
- [26] P.M.A. Areias, T. Belytschko, Analysis of three-dimensional crack initiation and propagation using the extended finite element method, *Int. J. Numer. Methods Engrg.* 63 (2005) 760–788.
- [27] P.M.A. Areias, J.M.A. César de Sá, C.A. Conceição António, J.A.S.A.O. Carneiro, V.M.P. Teixeira, Strong displacement discontinuities and Lagrange multipliers in the analysis of finite displacement fracture problems, *Computat. Mech.* 35 (2004) 54–71.
- [28] S. Ahmad, B.M. Irons, O.C. Zienkiewicz, Analysis of thick and thin shell structures by curved finite elements, *Int. J. Numer. Methods Engrg.* 2 (1970) 419–451.
- [29] P. Deuffhard, *Newton Methods for Nonlinear Problems, Affine Invariance and Adaptive Algorithms*, Springer, 2004.
- [30] M. Jirásek, Comparative study on finite elements with embedded discontinuities, *Comput. Methods Appl. Mech. Engrg.* 188 (2000) 307–330.
- [31] F. Armero, D. Ehrlich, Finite element methods for the multi-scale modeling of softening hinge lines in plates at failure, *Comput. Methods Appl. Mech. Engrg.*, in press, doi:10.1016/j.cma.2005.05.040.
- [32] J.E. Ash, T.J. Marciniak, Comparisons of finite-element code calculations to hydrostatically-loaded subassembly duct experiments, Technical Report ANL/RAS 75–31, Argonne National Laboratory, Reactor Analysis and Safety Division, 9700 South Cass Avenue, Argonne, Illinois 60439, August 1975.
- [33] A.L. Keesecker, C.G. Davila, E.R. Johnson, J.H. Starnes Jr., Crack path bifurcation at a tear strap in a pressurized shell, *Computers and Structures* 81 (2003) 1633–1642.
- [34] H.T. Budiman, P.A. Lagace, Nondimensional parameters for geometric nonlinear effects in pressurized cylinders with axial cracks, *ASME J. Appl. Mech.* 64 (1997) 401–407.
- [35] C.M. Muscat-Fenech, A.G. Atkins, Out-of-plane stretching and tearing fracture in ductile sheet materials, *Int. J. Fracture* 84 (1997) 297–306.